Development of Pulsed Current Arc Welding to Preclude Carbide Precipitates in Hastelloy X Weldment Using ERNiCr-3

M. Sathishkumar and M. Manikandan

In this study, gas tungsten arc (GTA) and pulsed current gas tungsten arc (PCGTA) welding on Hastelloy X were performed using ERNiCr-3. The welded plates are free from the porosity, inclusion, liquation cracks, and hot cracks. The weld bead profile shows a lower bead width in PCGTA than GTA weldment. The segregations of Cr, Mo, Nb, and Ti were identified in GTA with the development of Fe_3Mo_3C (M_6C), Fe_2MoC (M_3C), $Cr_{23}C_6$, Cr_2Ti, Ni_8Nb phases. While in PCGTA, Nb and Ti segregations alone were observed with the formation of phases like Ni_3Ti, Cr_2Ti, Ni_8Nb, respectively. The presence of γ prime precipitate (Ni_3Ti) observed in PCGTA improved the ultimate tensile strength (UTS) by 8.56% compared to GTA. The UTS and ductility were found inferior in both the weldments when compared to the base metal. This is due to the precipitation of Ni_8Nb phase and the existence of Cr_2Ti phase, respectively. The PCGTA weldment also shown improved microhardness by 12.21% and impact energy by 9.78% compared to GTA, respectively. The refined crystallite size and precluded carbide precipitates in PCGTA are responsible for the enhanced properties.

1. Introduction

The Ni-based superalloys are providing massive support in the aircraft industries with its outstanding properties at higher operating temperatures. Particularly, Hastelloy X is one of the Ni-based superalloys having Ni-Cr-Fe-Mo as the major elements, and it is fabricated by solid solution processing. It also gives excellent oxidation and corrosion resistance properties at higher temperature conditions. Hence, it has been utilized in aerospace parts like the combustion chamber, tails pipes, thrust reverser, boilers, gas turbine parts, and gas-cooled high-temperature reactor (Ref 1).

The developments of cracks were formed and propagated on the aerospace components due to the prolonged usage in a very high-temperature environment. These cracks can be resolved by selecting the permanent joining processes like welding, which could substantially save a tremendous amount of cost instead of parts replacement (Ref 2). The gas tungsten arc (GTA) welding is a kind of fusion welding method, which gives the cost-effective and best quality weldment than the other kind of arc welding technique. Further, the GTA welding of Hastelloy X is challenging due to the development of precipitation of secondary carbides, which decreases the tensile strength as well as develops hot cracks in the weldment (Ref 3, 4).

Sihotang et al. (Ref 5) evaluated the impact of minimum and maximum heat input on the tensile strength of the Hastelloy X weldment using AMS 5798 standard filler. The authors concluded that at high heat input conditions, low strength was obtained due to the low thermal gradient. It provides no time for the liquated phase at the dendritic boundary to dissolve back into the matrix. Hence, this promotes the development of the Mo-rich P phase, and the Cr-rich σ phase in the weldment. But, at low heat input conditions, high strength was obtained due to the steep thermal gradient providing enough time for carbides to dissolve back in the weldment. Both the cases, no liquation, or hot cracks were formed. Sihotang et al. (Ref 6) also reported fatigue strength and tensile properties of the shroud component made of Hastelloy X by Tungsten inert gas (TIG) welding using base metal filler. The occurrences of $M_{23}C_6$, σ, M_6C, and μ phases were detected in the weld zone (WZ). Also, the tensile fracture was found at the heat-affected zone (HAZ) for high heat supply.

Pakniat et al. (Ref 7) stated the impact of pulse frequency and pulse duration on the formation of hot cracks during Nd:YAG laser welding of Hastelloy X. The development of hot cracks in the weldment decreases with the increasing pulse frequency as well as duration. Also, the increase in heat input during the continuous mode of laser welding reduces the hardness value compared to pulse mode laser welding. Zhao et al. (Ref 8) developed the time-temperature-transformation (TTT) graph for the various carbides such as $M_{23}C_6$, σ, P, and M_6C. The development of M_6C and σ phases was found at the temperature of around 900 °C, whereas the μ phase was formed at the temperature between 800 and 980 °C. Reza Abedi et al. (Ref 9) studied the one time, two times, and three-times welding of the Hastelloy X. Authors concluded the occurrence of Cr-rich $M_{23}C_6$ and Mo-rich M_6C carbides and the dendrite arm spacing of $M_{23}C_6$ was larger than M_6C carbide. Also, the third time welding provided the highest ultimate tensile strength (UTS) with respect to the first and second time of welding.

M. Sathishkumar and **M. Manikandan**, School of Mechanical Engineering, Vellore Institute of Technology, Vellore 632014, India. Contact e-mails: desingsathish@gmail.com and mano.manikandan@gmail.com.

Manikandan and Sivakumar et al. (Ref 10) evaluated the effect of shielding gas for continuous and compound current pulsed GTA of Inconel 718. They determined that the steeper thermal gradient and speedy cooling rate observed in pulsed GTA reduces the growth of secondary precipitates in the weld region compared to the low cooling rate and minimum thermal gradient obtained in constant current GTA welding. Subramani et al. (Ref 11) developed the pulsed current technique to preclude the Cr-rich precipitates in Nimonic 80A. They also evaluated the influence of GTA as well as PCGTA welding on the development of $Cr_{23}C_6$ precipitate for ERNiCrMo-3. The development of $Cr_{23}C_6$ precipitate was found in the GTA welding, and it was absent in the PCGTA. Arulmurugan et al. (Ref 12) investigated the influence of Mo-rich carbides on GTA and PCGTA welding technique for Inconel 686. In PCGTA, the enhanced ductility, ultimate tensile strength, and yield strength were observed with respect to GTA. The occurrence of Mo-rich precipitates in the GTA was pulled down, its mechanical properties.

From the literature, it is essential to select the welding technique to eliminate the hot cracks in the Hastelloy X by precluding the development of secondary carbides (Mo-rich and Cr-rich). The major elements like Mo, Cr, form the intermetallic $M_{23}C_6$, M_6C, σ, and P phases in the weldment region, and it also begins and propagates the hot cracks while welding. These precipitates also minimize the UTS and microhardness of the weldment. The proper selection of the welding method and appropriate welding parameters controls the development of hot cracks. The versatile availability and best quality of welding can be obtained by using GTA welding methods. In this work, the comparative study of GTA and PCGTA welding is investigated using ERNiCr-3 filler. The Nb element in the filler wire tends to develop Nb precipitates instead of providing carbon to form Mo and Cr carbide precipitates. It is expected that severe segregation of carbide precipitates can be minimized by using ERNiCr-3 filler wire. The minimum heat input utilized in the pulsed mode alleviates the development of hot cracks in the weld joint. The pulsed current GTA welding is believed to preclude the microsegregation of Cr-rich and Mo-rich precipitates in the weld joints of various superalloy grades. Hitherto, there is no research work available for suppressing $M_{23}C_6$, σ, P, and M_6C precipitates in the weldments of Hastelloy X joined using GTA and PCGTA welding methods. The purpose of the present research is to minimize the heat input supplied by adapting the PCGTA, which decreases the hot cracking tendency by suppressing the secondary carbide phases. It also increases the mechanical properties of the weldment compared to GTA weldment. The defect-free and better property weldments achieved in this work can be directly utilized by industry application.

2. Experimental Procedure

2.1 Welding of Hastelloy X

The size of 500 mm × 500 mm × 7 mm thick plate of Hastelloy X was obtained in solution annealed condition, and ERNiCr-3 filler of 1.2 mm diameter was bought in rod form. The received plate and filler were tested with optical emission spectroscopy (OES) to identify the elemental weight percentage. The nominal composition (in wt.%) of Hastelloy X is 48.68Ni, 22.34Cr, 18.15Fe, 9.16Mo, 0.875Co, 0.264Si, and 0.247Mn (W, C, P, and S are less than 0.2%). The nominal composition (in wt.%) of ERNiCr-3 filler wire is 72.79Ni, 18.22Cr, 3.00Fe, 2.50Mn, 2.0Nb, 0.75Ti, and 0.5Si (C, and S are less than 0.1%). The surface of the plate was cleaned using acetone to take away the impurities, oils, and other foreign particles. The wire-EDM (electrical discharge machining) was utilized to cut the received plate to a size of 170 mm × 55 mm × 7 mm. The single V-shaped groove profile of an angle 60° (each plate has the bevel angle of 30°), root gap of 1.2 mm, root face of 0.8 mm was produced on the plate using the milling machine. The acid pickling process was carried out using a mixture of HCl and distilled water environment by dipping the plates for 15 min to wash the foreign particles on the surface.

The samples were fixed using C-Clamp on the work-table over the copper plate to arrest the distortion. The direct current electrode negative (DCEN) was used for GTA as well as PCGTA welding using ERNiCr-3, and the complete penetration was observed in four passes using KEMPI GTA welding (Model: DWE 400 AC/DC) equipment. The welding was done in the argon shielded environment with a supply of 15 L/min to control the interaction of atmospheric air with the molten metal. It also provides less disturbance for an arc to travel from electrode to the workpiece and releases the work function on the workpiece in the form of heat, which melts both the plate and filler wire. During welding, the time taken for a complete length of 170 mm was noted down to calculate the welding travel speed. The surface after each pass was cleaned to eliminate the oxide layer, and the physical quality of weld was excellent (no hot cracks in the WZ) in both weld joints. The welded Hastelloy X with ERNiCr-3 photographs is presented in Fig. 1.

The heat input required for welding was determined with input voltage (V), input current (I), welding efficiency (η), and welding travel speed (S). The mean current (I_{mc}) was used for calculating heat input in case of PCGTA method of welding. Equation 1 and 2 provided the mean current and heat input of single-pass (Ref 13, 14). Finally, the total heat input was calculated by taking the sum of all four passes, and the value of welding parameters and total heat utilized are given in Table 1.

The mean current (I_{mc}) is determined by,

$$I_{mc} = \frac{(I_{pc} \times t_{pc}) + (I_{bc} \times t_{bc})}{t_{pc} + t_{bc}} \text{ in (A)} \quad \text{(Eq 1)}$$

The heat input (H_s) is given by,

$$H_s = \eta \times \frac{I_{mc} \times V}{S} \text{ in (kJ/mm)} \quad \text{(Eq 2)}$$

whereas, I_m—mean current (A), I_{bc}—base current (A), t_{bc}—base current duration (s), I_{pc}—peak current (A), t_{pc}—peak current duration (s), H_s—heat input supplied in a pass (kJ/mm), η—melting efficiency (0.7), V—welding voltage (v), S—welding speed (mm/s).

2.2 Metallurgical Studies

The milling was carried out to remove the top projection of the weld bead from the surface of the weldments. The coupons of size 10 mm × 10 mm × 7 mm were cut into the perpendicular direction of weld to study the metallurgical properties of the weldment. The skeleton of coupons extracted for various
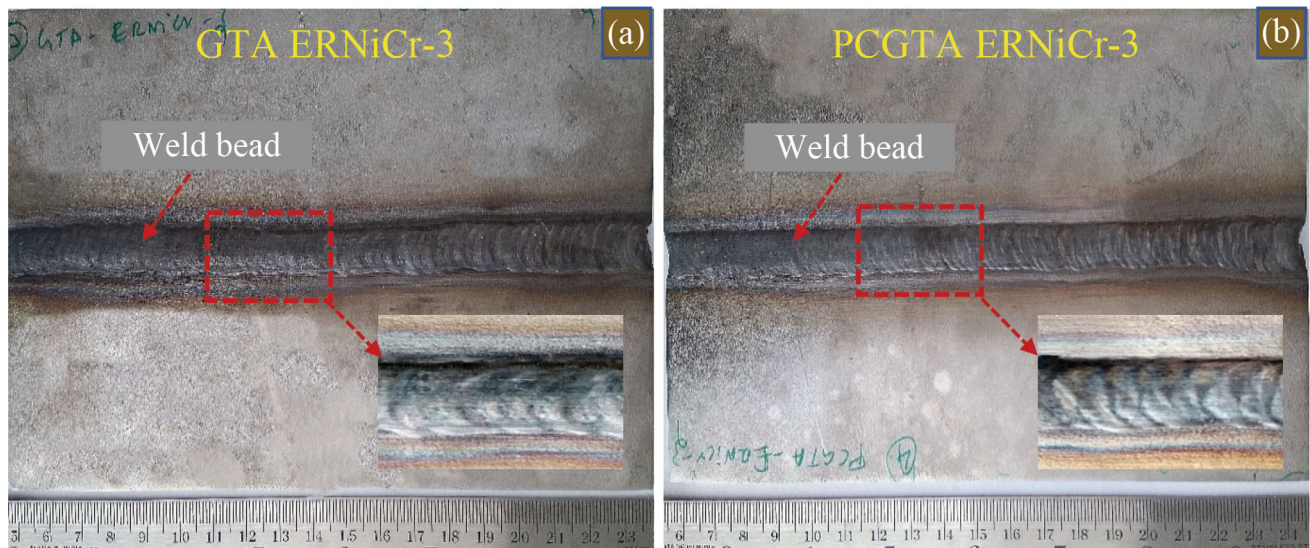
Fig. 1 Welded plates photograph of Hastelloy X welded using ERNiCr-3 by; (a) GTA Welding (b) PCGTA Welding

Table 1 Process parameters of GTA and PCGTA with ERNiCr-3

| Welding Methods and filler metals	Name of pass	Constant, peak, base current (I_{cc}, I_{bc}, I_{pc}) in, A	Voltage, V in Volts	Welding travel speed, S in mm/s	Heat supplied in each pass, H_s in kJ/mm	Total heat supplied, H_{ts} in kJ/mm
GTA	Root	120 (I_{cc})	11.4	1.10	0.872	3.479
ERNiCr-3	First	120 (I_{cc})	11.4	0.99	0.968	
	Second	120 (I_{cc})	11.4	1.18	0.814	
	Third	120 (I_{cc})	11.4	1.16	0.825	
PCGTA	Root	120 (I_{pc}) 60 (I_{bc})	9.4	0.800	0.740	3.086
ERNiCr-3	First	120 (I_{pc}) 60 (I_{bc})	9.4	0.776	0.763	
	Second	120 (I_{pc}) 60 (I_{bc})	9.4	0.690	0.859	
	Third	120 (I_{pc}) 60 (I_{bc})	9.4	0.818	0.724	
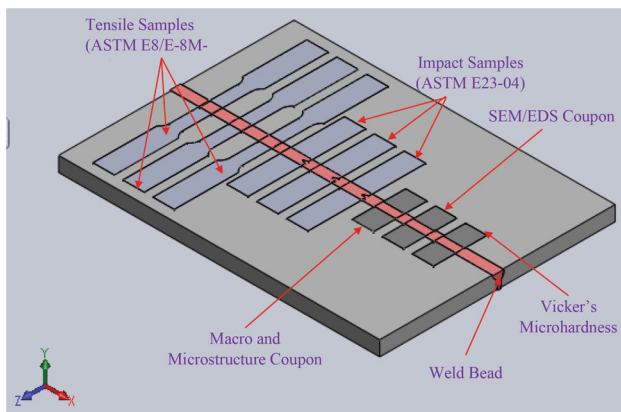
Fig. 2 Layout of extracted coupons of Hastelloy X weldment for different studies

testing is shown in Fig. 2. The hot press mounting machine was utilized to mount the coupons using bakelite powder. The hand polishing of coupons was done on different emery sheets beginning from 220 to 2000 grit size. Then, the coupons were polished using a disk polishing machine using alumina and water at a speed of 450 rpm to obtain a mirror-like finish. The

mixture of 10 g oxalic acid along with 100 ml distilled water was used as an etchant. The weldment was electrolytically etched for 10–15 s using 12 V direct current to reveal the microstructure.

The AM1145T Dino-Lite-Edge digital macroscope was utilized to capture the macrostructure of the weldment. The macrostructures of both the GTA and PCGTA weldments reveal that defects like hot cracks, undercut, porosity, insufficient fusion, excess inclusion in both weldments were absent (Fig. 3a and b). The low heat input (3.086 kJ/mm) employed in PCGTA reduces the Marangoni convection, and less shear stress brought by plasma jet causes the low outward surface tension in the weld pool. This decreases the width of the weld bead compared to high heat input (3.479 kJ/mm) supplied during GTA.

The microstructure of weldments was captured at the weld interface and weld center region by the optical microscope made of ZEISS. The scanning electron microscopy (SEM) and energy dispersive spectroscopy (EDS) were done to evaluate the precipitation of secondary phases, and the elemental weight percentage of alloying elements at the dendritic and interdendritic zone in both the weld center and weld interface region. The chemical compound of the secondary precipitates in the weldment was evaluated using an x-ray diffraction (XRD) test by BRUKER D8 advanced XRD machine. From the XRD
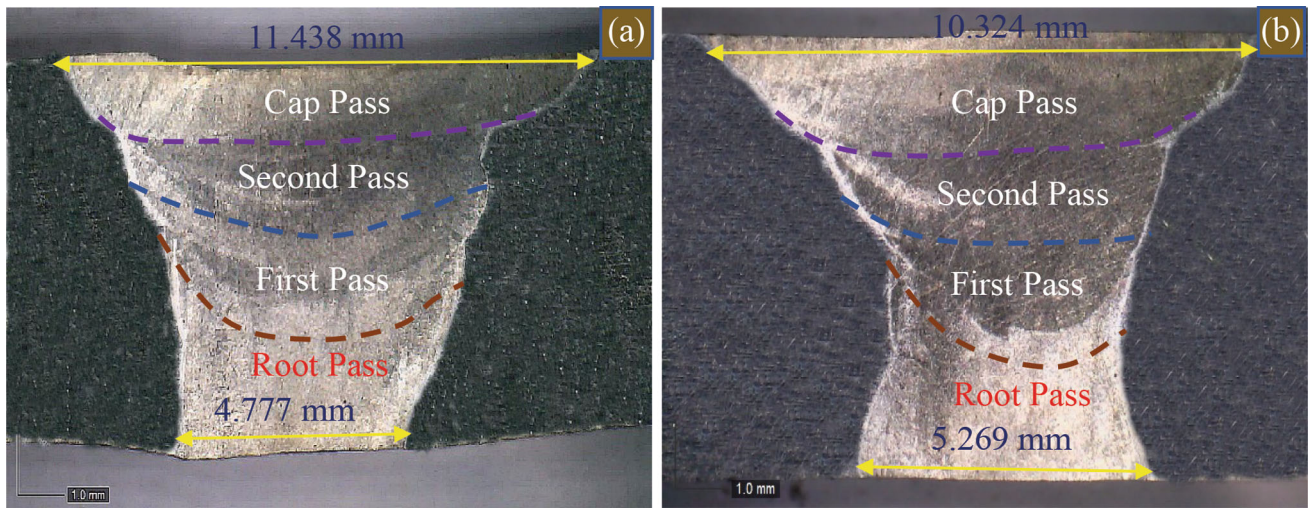
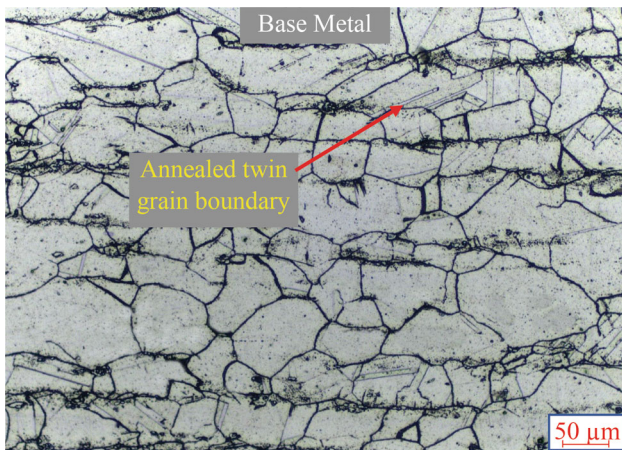**Fig. 3** Macro photograph of Hastelloy X welded using ERNiCr-3 by; (a) GTA (b) PCGTA

Fig. 4 Microscale photograph of as received Hastelloy X

analysis, the calculation of dendrite arm spacing of weldment was determined from Scherer's formula.

2.3 Mechanical Testing

The percentage of elongation, UTS, 0.2% of proof strength of welded coupons was measured by following the ASTM standard of E8/E-8M-13a using INSTRON 8801 machine (crosshead speed of 2 mm/min) at ambient condition. The impact toughness was performed for the coupons having the notch of 2 mm depth and groove angle of 45° as per the ASTM E23-04 on Charpy's impact testing machine (Model: FIT 300-O pendulum). The type of fracture in both impact and tensile testing was determined by SEM fractography analysis. The Vicker's microhardness of the coupons was measured in both base metal and weldment region with an interval of 0.25 mm, dwell time of 10 s, a load of 500 gf.

3. Results and Discussion

3.1 Microstructure

The optical microstructure of received Hastelloy X plate in solution annealed condition is exposed in Fig. 4. It reveals the austenite phase in the face-centered cubic (FCC) matrix. The weldment microstructures are studied for each pass, namely root pass, first pass, second pass, and third pass. The microstructure of all passes for GTA and PCGTA is exposed in Fig. 5(a), (b), (c), (d), (e) and 6(a), (b), (c), (d), (e), respectively. No cracks were found in the weldments for both cases. The cap and root passes of GTA and PCGTA reveal the columnar dendrite (Fig. 5a and d, 6a and d). The formation of columnar dendrite is believed to be the development of microstructural growth and directional growth of nuclei which is determined by the direction of heat extraction (Ref 15). The second and first pass of PCGTA reveals the fine equiaxed dendrite (Fig. 6b and c), whereas GTA shows the cellular dendrite (Fig. 5b and c) (Ref 16-18).

The high heat supply develops the larger dendritic arm spacing in GTA, and low heat supply in PCGTA develops the lower dendrite arc spacing (Ref 19). The variation of input current from peak to base in PCGTA controls the total amount of heat supplied, which can be governed by the following parameters (1) repeated temperature change, (2) better fluid flow, (3) steeper thermal gradient, (4) rapid cooling rate. The diffusion rate gets decreases in the case of PCGTA welding due to low temperature or steeper thermal gradient, and this will not allow nucleated particles to grow, which causes the finer dendrites spacing. A similar kind of refinement in the dendrites spacing was also observed by other researchers (Ref 20-22).

The effect of liquation cracks can be controlled by the size of HAZ, which mainly depends on the heat supply. In PCGTA weld joint, the size of HAZ is lesser compared to GTA. The reduction in the HAZ size is due to the steeper thermal gradient,
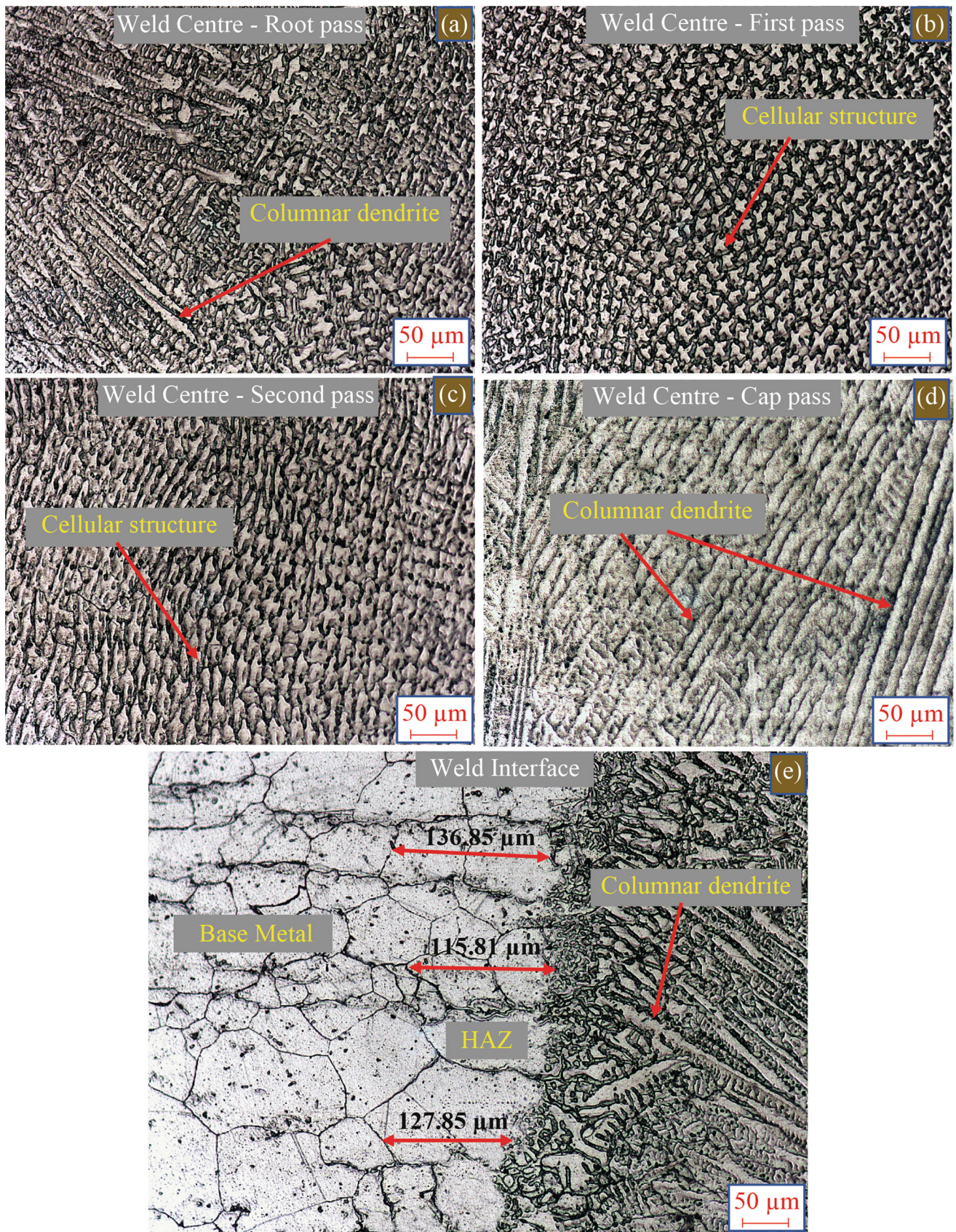
Fig. 5 Microstructure of GTA weldment with ERNiCr-3 at (a) Root (b) First (c) Second (d) Cap (e) Interface
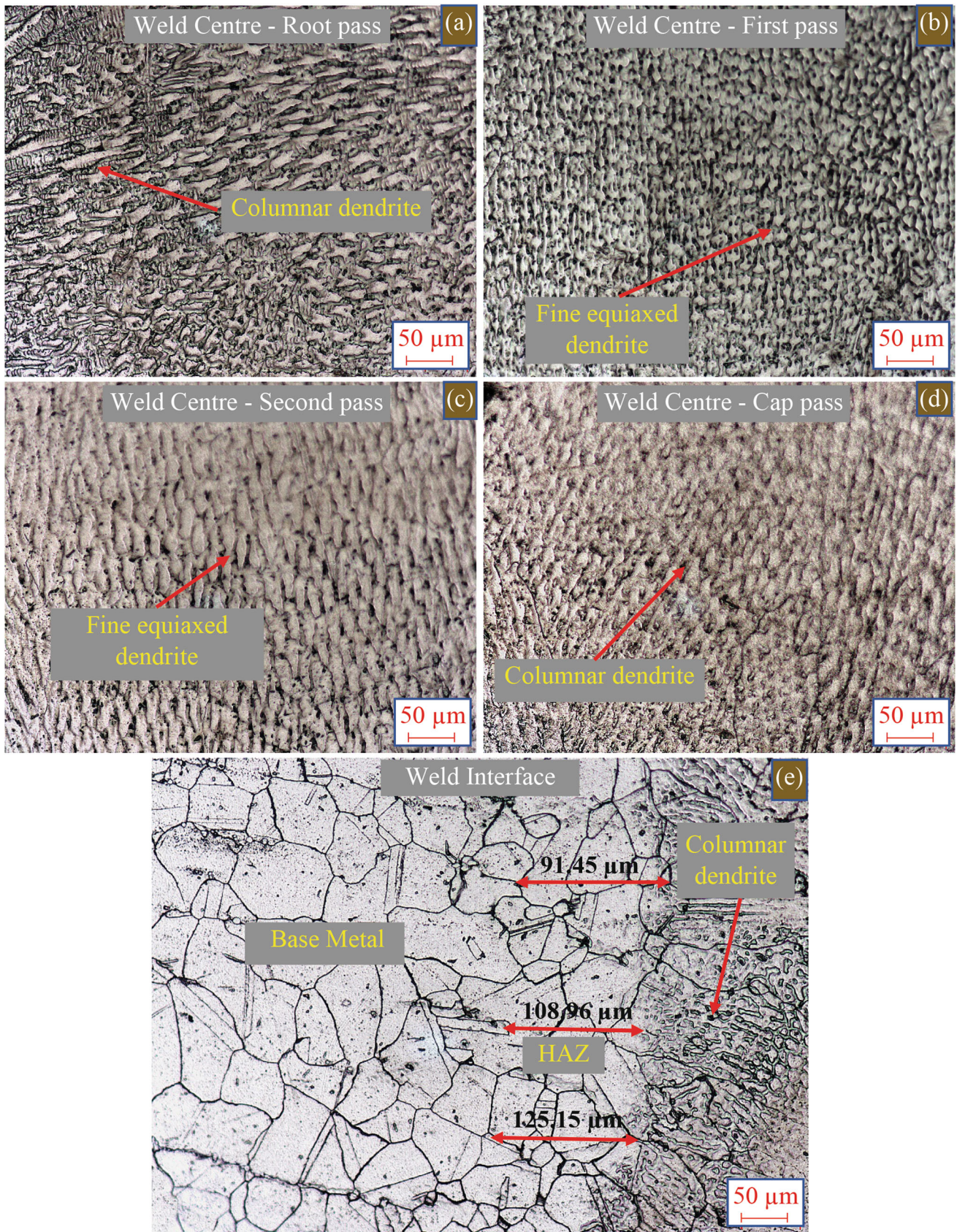
Fig. 6 Microstructure of PCGTA weldment with ERNiCr-3 (a) Root (b) First (c) Second (d) Cap (e) Interface

rapid cooling rate, and minimum heat provided during PCGTA. The larger HAZ size in GTA promotes more changes in the formation of secondary precipitates which cause liquation cracks in the weldment, and also reduces the mechanical properties. In both GTA and PCGTA, no such cracks are formed in the HAZ region. It is believed that the welding parameters obtained in this work are optimum to obtain the crack-free weld joint.

3.2 Microsegregation

The existence of Cr-rich and Mo-rich phases during the final stage of solidification causes the hot cracks in the weldment. The scanning electron microscopy (SEM) of GTA and PCGTA in the weld center and interface area are presented in Fig. 7 and 8(a) and (b). The results reveal finer dendrite arm spacing in PCGTA weldment and coarser dendrite arm spacing in GTA weldment. This refined dendrite arm spacing has a more dendritic boundary area, and it provides low free energy which reduces the formation of new secondary precipitates (Ref 21, 23). Whereas in case of GTA weldment, the coarser dendrite arm spacing is observed, which increases the available free energy at the dendritic boundary, and it promotes the development of new secondary precipitates. Other researchers also stated a similar kind of observation (Ref 12, 16).

The elemental segregation (wt.%) of elements in weld center and weld interface regions are evaluated using EDS (Table 2 and 3). The EDS evaluation of GTA and PCGTA weld joints are given in Fig. 7 and 8(i-iv). The microsegregation of Cr-rich carbide, Mo-rich carbide, Ti, and Nb precipitates are identified in the interdendritic zone of GTA weldment. In the case of PCGTA weldment, only Ti, and Nb precipitates are identified in the interdendritic zone (Ref 24). The developments of Cr-rich and Mo-rich carbide precipitates are detected when it has a sufficient amount of Mo, Cr, and C element as well as exposed to higher temperatures for a certain period, which causes the depletion of Mo and Cr around the dendritic boundary (Ref 25). The highest temperature in the weld center of GTA weldment causes this carbide precipitation. The same is not identified in PCGTA weldment due to low temperature in the weldment compared to GTA. Many researchers found similar segregation of Cr-rich and Mo-rich precipitates in GTA (Ref 11, 12, 16, 26).

3.3 Phase Analysis

The identification of compound precipitates is evaluated using XRD. The variation in the intensity of different precipitates with respect to 2θ for base metal, GTA, and PCGTA weld joints are displayed in Fig. 9. The GTA weldment exposed the development of Fe_3Mo_3C (M_6C), Fe_2MoC (M_3C), $Cr_{23}C_6$, Cr_2Ti, and Ni_8Nb precipitates, whereas PCGTA weldment revealed the development of Ni_3Ti, Cr_2Ti, Ni_8Nb precipitates (Ref 27). The occurrence of Mo-rich and Cr-rich carbide phases is not observed in PCGTA weldment because of the steeper thermal gradient and speedy cooling rate. In addition to it, low heat input does not provide the required period for the growth of new nuclei (Ref 16). The peak shift information of 2θ depicts that all the observed peaks of PCGTA

weld joint are marginally shifted when compared to GTA. The peak shift differences are determined from left side to right, and the shift of 0.020°, 0.178°, 0.509°, and 0.159° are observed in PCGTA compared to GTA (Fig. 9). The change in the lattice strain is mainly attributed to the peak shift in PCGTA and GTA weldment. Also, the higher peak intensity observed in GTA promotes the higher amount of segregation of precipitates compared to the PCGTA weldment. The full width half maximum (FWHM) is calculated using the peak intensity and 2θ angle for XRD analysis. The dendrite arm spacing of the weldments is determined by a gaussian method using Scherrer's formula (Ref 11) (Eq 3).

Dendrite arm spacing,

$$D = \frac{c\lambda}{\beta \cos \theta} \text{ in nm} \tag{Eq 3}$$

whereas D—mean dendrite arm spacing (nm), θ—diffraction angle (degree), λ—wavelength of x-ray (1.54×10^{-10} m), β—full width half maximum (FWHM) (radiant), c—dimensionless shape factor (0.94). The dendrite arm spacing of GTA weldment is 24.15 nm, and PCGTA weldment is 22.43 nm. The PCGTA weldment shows the 7.64% reduction in dendrite arm spacing with respect to GTA weldment.

3.4 Tensile Properties

The mean of, % elongation, UTS, 0.2% of proof strength of weldment are analyzed through tensile testing. The test results of base metal, GTA, and PCGTA weld joints are given in Table 4. The fractured images of specimens are illustrated in Fig. 10(a) and (b). It is clear that the lower ductility and strength values are found in GTA weldment than the base metal and PCGTA weldment. This lower strength can be attributed to the occurrence of secondary carbide precipitates in the GTA weld joint. The occurrence of Cr-rich and Mo-rich carbides such as Fe_3Mo_3C (M_6C), Fe_2MoC (M_3C), $Cr_{23}C_6$, and Ni_8Nb precipitates decreases the UTS and % elongation at the breakpoint in GTA weldment (Ref 9, 16, 28). The nonexistence of the Mo-rich and Cr-rich carbides precipitates, as well as the development of γ prime precipitates like Ni_3Ti, increase the UTS and ductility of the PCGTA weld joint over GTA (Ref 29). The existence of Ni_8Nb precipitates in PCGTA weldment decreases the % elongation and strength of the weld joint with respect to the base metal. The dendrite arm spacing refinement of 7.64% found in PCGTA weldment with respect to GTA is believed to be another reason for increases in strength (Ref 11).

Further, the weld joint efficiency was evaluated based on the ratio of weldment UTS value to the base metal, in order to determine the quality of the weldment. The joint efficiency results are shown 85.06 and 91.52% for GTA and PCGTA weldment, respectively. This concludes the better weld quality in PCGTA over GTA. The lower % elongation detected in GTA, as well as PCGTA weldment, is due to the existence of Cr_2Ti precipitates. Other studies also reveal the similar Cr_2Ti phase and its poor plasticity in weldment (Ref 30). The type of fracture of the weldment is evaluated through the SEM fractography analysis (Fig. 11a and b). In detail, characterization of the tensile fractured surface confirmed the presence of
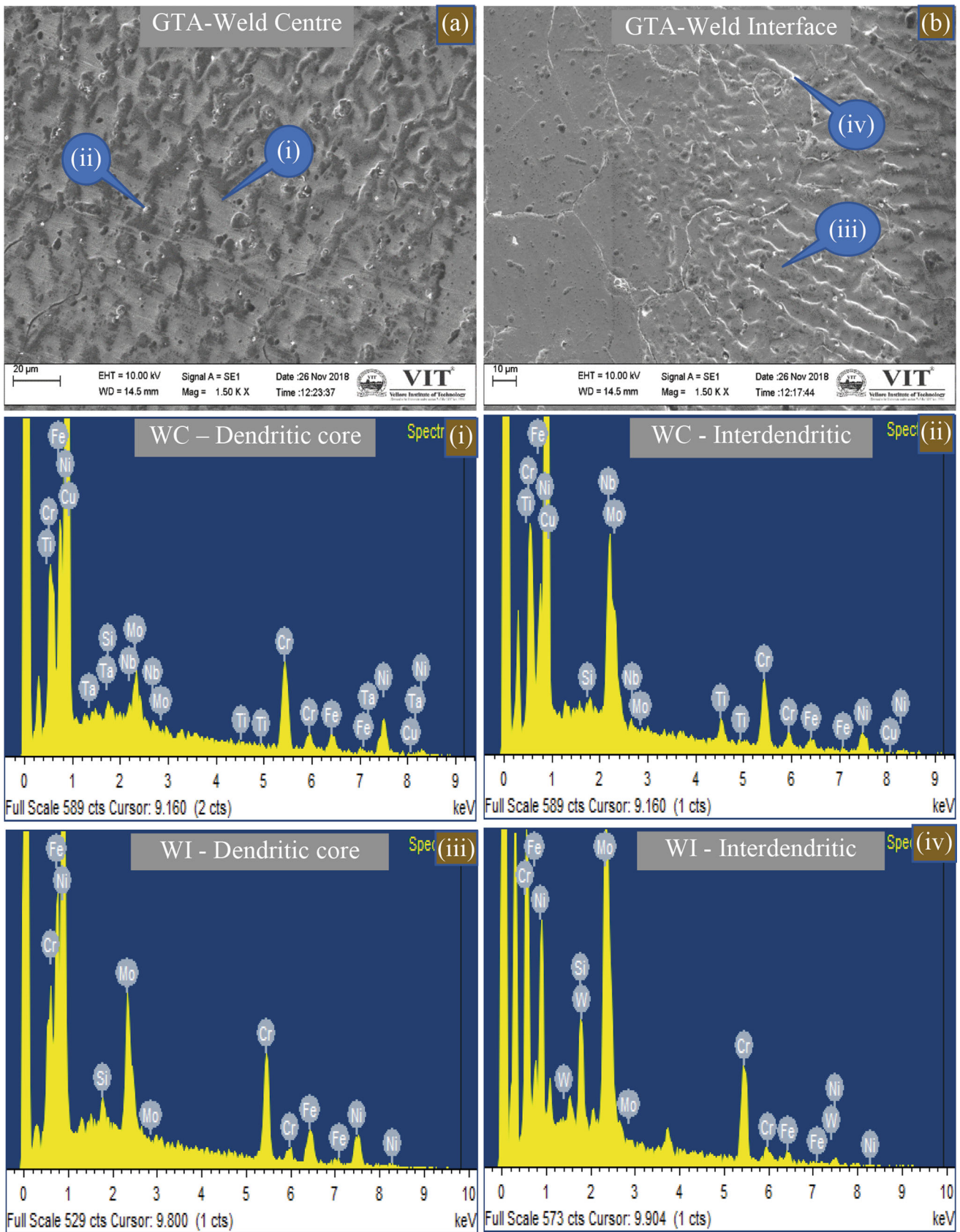
Fig. 7 SEM/EDS photographs of GTA ERNiCr-3 at; (a) Weld center (WC) (i) WC- dendritic core (ii) WC—interdendritic (b) Weld interface (WI) (iii) WI-dendritic core (iv) WI-interdendritic
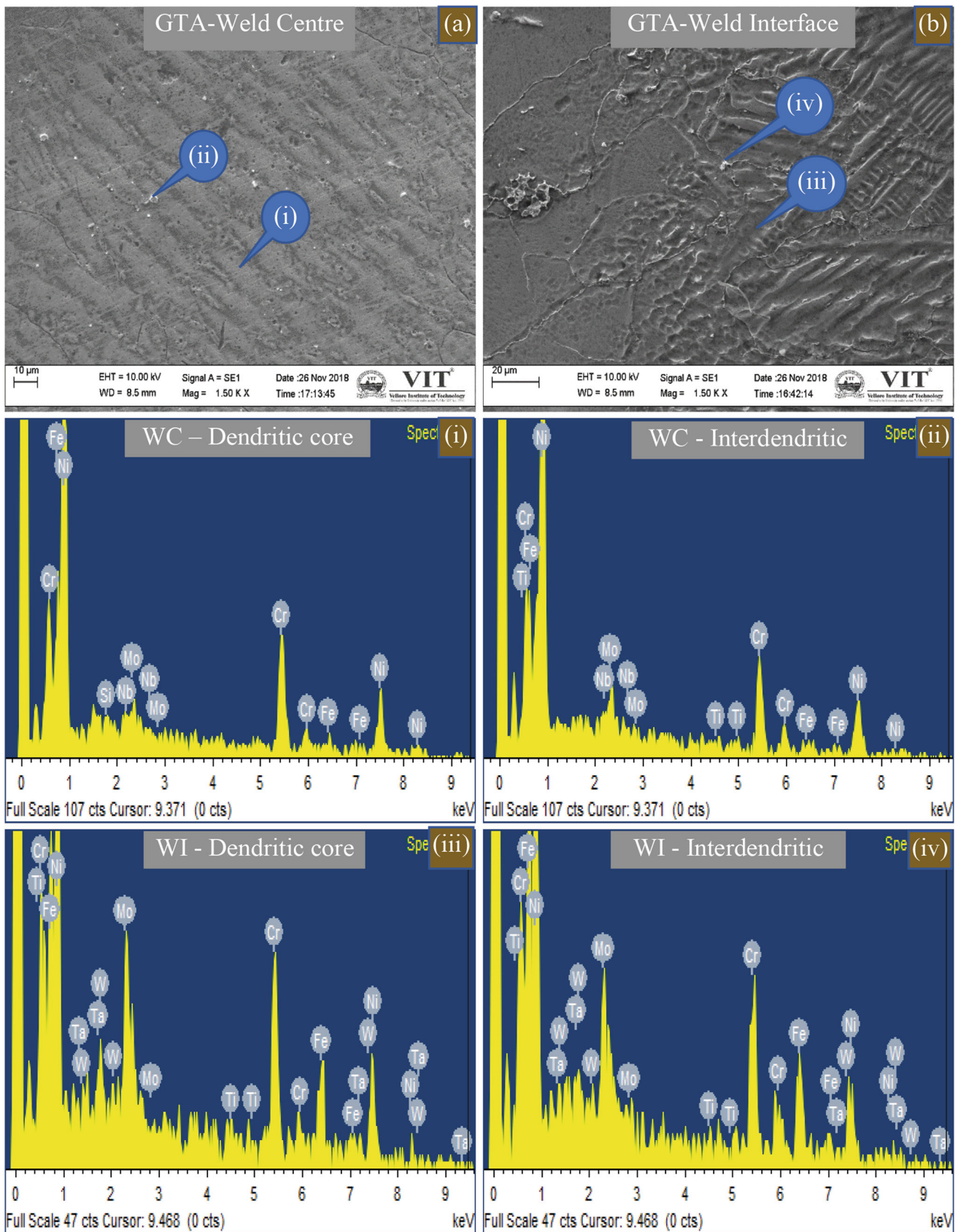
Fig. 8 SEM/EDS photographs of PCGTA ERNiCr-3 at; (a) Weld center (WC) (i) WC- dendritic core (ii) WC—interdendritic (b) Weld interface (WI) (iii) WI-dendritic core (iv) WI-interdendritic

Table 2 EDS values of GTA welded Hastelloy X using ERNiCr-3 filler at weld center and interface (wt.%)

S. no	Region		Ni	Cr	Fe	Mo	Ti	Si	Nb
1	Weld center	Dendritic core	59.51	23.86	9.53	3.05	0.21	0.07	1.64
2		Interdendritic	52.58	28.88	5.29	19.78	2.09	0.31	4.39
3	Weld Interface	Dendritic core	50.41	20.81	18.75	8.73	0.68	0.21	0.41
4		Interdendritic	15.9	44.69	9.43	25.4	1.29	0.44	2.84

Table 3 EDS values of PCGTA welded Hastelloy X using ERNiCr-3 filler at weld center and interface (wt.%)

S. no	Region		Ni	Cr	Fe	Mo	Ti	Si	Nb
1	Weld center	Dendritic core	67.99	20.36	7.58	2.25	0.20	0.51	1.32
2		Interdendritic	61.25	20.03	8.21	3.41	2.44	0.40	4.27
3	Weld Interface	Dendritic core	46.05	24.24	22.18	4.82	0.38	0.20	0.54
4		Interdendritic	44.39	24.91	18.27	7.21	1.24	0.32	3.65

the very fewer cleavage-facet, larger ductile dimples, and ductile tear ridges for GTA and PCGTA weld joints. The shapes of ductile dimples are observed in a heterogeneous manner. The size of ductile dimples in GTA weldment is larger than the PCGTA weldment. Hence, the low shape of ductile dimples and ductile tear ridges are primarily attributed to the higher strength and ductility in PCGTA over GTA. Also, the presence of these phases (ductile dimples and ductile tear ridges) are established the ductile kind of fracture.

3.5 Microhardness

The resistance to deformation of weldment is measured using Vicker's microhardness test, and results are plotted in a graph with respect to distance from the weld center (mm) (Fig. 12). The values of hardness are measured for three different zones of the weldment, such as base metal, HAZ, and weld center. The sudden peaks and valley are observed in some reading of microhardness graph for both GTA and PCGTA weldment. This is due to the coverage of single-phase by the microhardness indenter, which might have higher or lower microhardness than other zones. Further, in order to determine the cumulative effects of each reading in different zones such as base metal and weldment, the average microhardness has been calculated. The average hardness values for base metal, GTA weldment, and PCGTA weldment are 253.5 ± 8.1, 203.0 ± 7.3, 227.8 ± 9.2 HV, respectively. The change in the microstructure, development of precipitates, and variation in crystallite size in weldment are primarily attributed to the lower microhardness in GTA and PCGTA weldment than the base metal. The lower heat supply, steep thermal gradient, and

rapid cooling rate in PCGTA weldment provided 12.21% higher average microhardness than GTA. The development of γ prime strengthening precipitate such as Ni_3Ti, and 7.64% reduction in the dendritic arm spacing is mainly attributed to the improved microhardness in PCGTA weldment. The outcomes of the microhardness study are in-line with tensile test reports (Ref 31).

3.6 Impact Toughness Properties

The energy absorbed by the weldment before the sudden fracture is determined by the Charpy impact test, and it is given in Table 4. The PCGTA weldment provided improved toughness of 21.40% with respect to the base metal and 9.78% compared to GTA weldment, respectively (Ref 32). The coarser dendrite arm spacing and development of secondary precipitates (Fe_3Mo_3C (M_6C), Fe_2MoC (M_3C), $Cr_{23}C_6$) in the GTA weldment reduces impact toughness with respect to PCGTA (Ref 27). The enhanced toughness observed in the PCGTA is due to the absence of the secondary carbide precipitates, refined dendrite arm spacing, and formation of the γ prime strengthening phase (Ni_3Ti), with respect to the base metal and GTA weldment (Ref 33). The impact toughness fractured samples are studied through the SEM fractography to evaluate the type of failure (Fig. 13). The presence of a larger number of ductile dimples, ductile tear ridges, and cleavage-facet are indicated the ductile kind of failure. Also, the heterogeneity in the dimple shape further confirmed the ductile kind of failure in both GTA and PCGTA weldment. Thus, the impact test results are in-line with tensile test and microhardness analysis (Ref 12).

1. Mo_1Ni_4, 2. Fe_3Mo_3C (M_6C), 3. Cr_2Ti, 4. Ni_8Nb, 5. Fe_2MoC (M_3C),
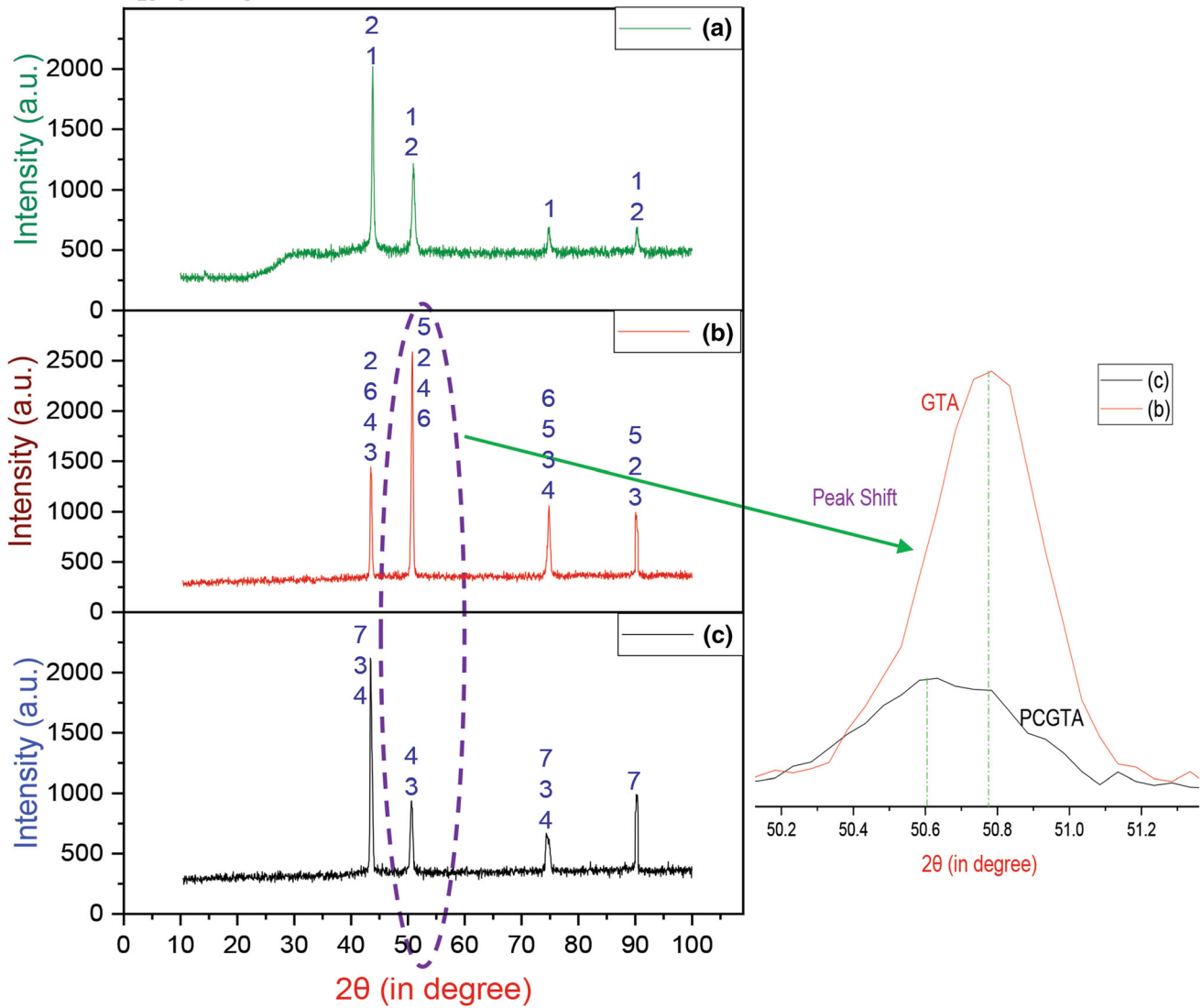
6. $Cr_{23}C_6$, 7. Ni_3Ti

Fig. 9 XRD graph of; (a) Base metal (b) GTA—ERNiCr-3 (c) PCGTA—ERNiCr-3

Table 4 Tensile properties of Hastelloy X weldment by GTA and PCGTA techniques with ERNiCr-3

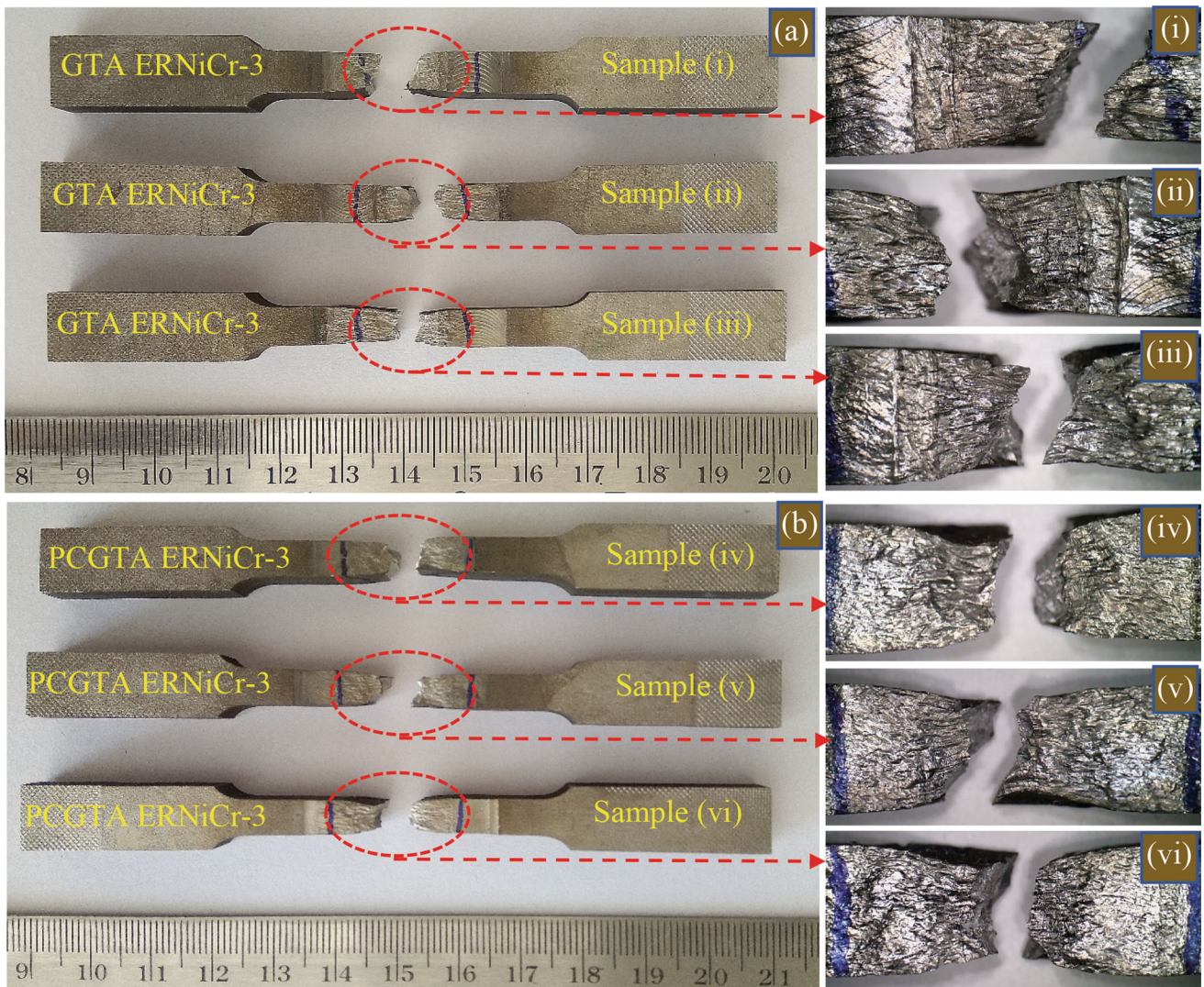| Materials	Mean UTS, MPa	Mean 0.2% proof strength, MPa	Mean ductility, %	Average impact toughness absorbed, J
Base material	790 ± 3.1	322 ± 8.5	46 ± 0.6	57.9 ± 1.8
GTA ERNiCr-3	666 ± 4.0	334 ± 2.3	26 ± 3.1	64.1 ± 1.6
PCGTA ERNiCr-3	723 ± 4.7	366 ± 6.1	32 ± 1.2	70.4 ± 1.5

Fig. 10 Photographs of tensile fractured coupons welded by (a) GTA—ERNiCr-3 (b) PCGTA—ERNiCr-3
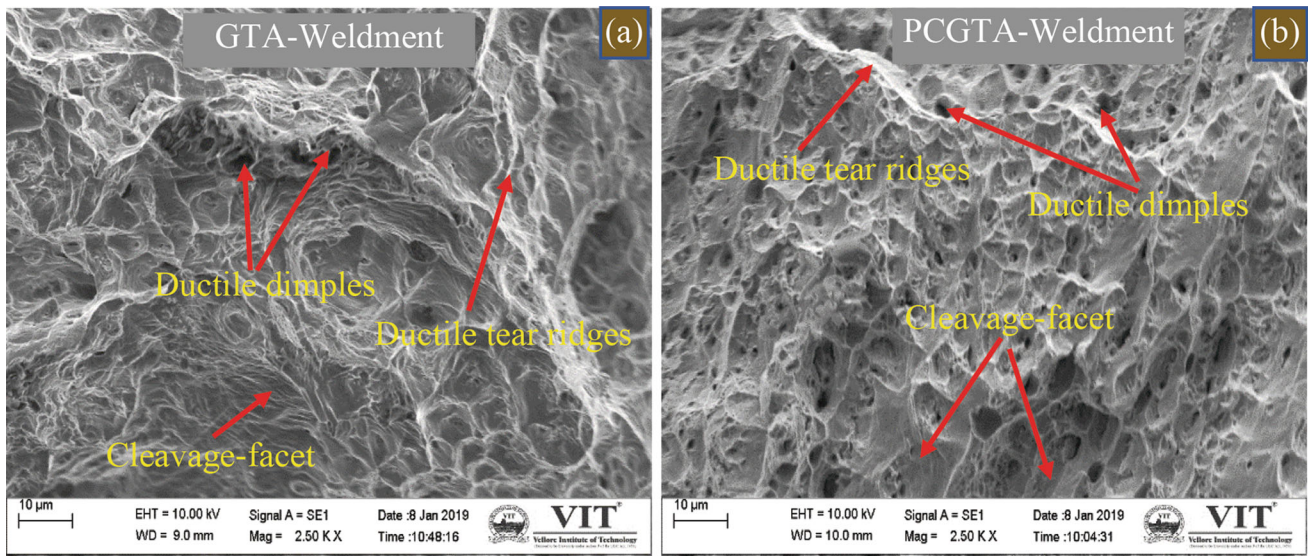

Fig. 11 SEM fractography of tensile fractured coupons welded by (a) GTA—ERNiCr-3 and (b) PCGTA—ERNiCr-3

4. Conclusions

1. The welding of PCGTA and GTA are completed without any inclusions, porosity, hot cracks, and liquation cracks in the weldment. The PCGTA weldment provided the shorter bead width with respect to GTA.
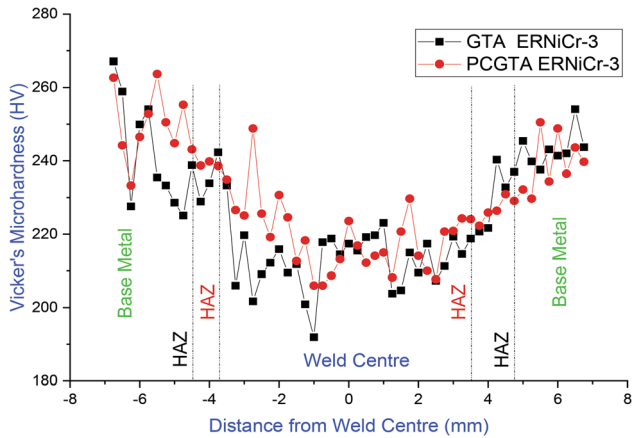

Fig. 12 Vicker's Microhardness value GTA and PCGTA weldment—ERNiCr-3

2. The direction of heat extraction causes the columnar dendrites in both GTA and PCGTA weld joints for cap and root pass. The low heat supply in PCGTA weldment forms the equiaxed dendritic structure for the first and second pass, whereas cellular structure is observed in GTA weldment.

3. The segregation of Mo, Cr, Nb, and Ti was observed in GTA weldment, but only Nb, Ti segregation is recognized in PCGTA. The occurrence of Mo and Cr-rich precipitates is removed in PCGTA weldment because of the steeper thermal gradient and speedy cooling rate exhibited.

4. The existence of Fe_3Mo_3C (M_6C), Fe_2MoC (M_3C), $Cr_{23}C_6$, Cr_2Ti, and Ni_8Nb precipitates is found in GTA weld joint. Whereas in PCGTA weld joint, the formation of Ni_3Ti, Cr_2Ti, and Ni_8Nb precipitates are observed. The refinement of 7.64% in dendrite arm spacing is observed in PCGTA over GTA weldment.

5. The existence of γ prime strengthening precipitates (Ni_3Ti) improved the UTS of PCGTA weldment (8.56%) when compared to GTA. The exhibition of Cr_2Ti precipitates decreases the strength of both GTA and PCGTA compared to the base metal.

6. The PCGTA provides an improved impact toughness of 21.40 and 9.78% with respect to the base metal and GTA. Also, the PCGTA weldment shown 12.21% of improved microhardness compared to GTA. The refinement in the dendrite arm spacing improves the impact toughness and microhardness.
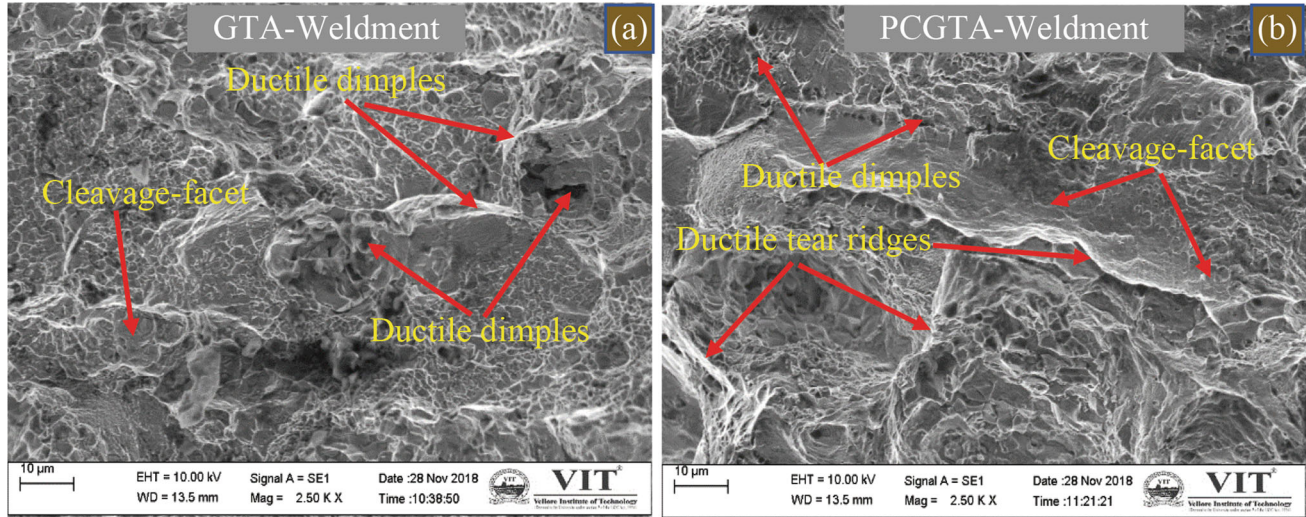

Fig. 13 SEM fractography of toughness coupons welded by (a) GTA—ERNiCr-3 and (b) PCGTA—ERNiCr-3

References

1. Inconel alloy HX (UNS N06002), Technical Data Sheet, Special Metal Corporation (2005). http://www.specialmetals.com/assets/smc/documents/alloys/inconel/inconel-alloy-hx.pdf. Accessed 8 Aug 2019
2. L. Rakoczy, M. Grudzien, L. Tuz, K. Pancikiewicz, and A. Zielinska-Lipiec, Microstructure and Properties of a Repair Weld in a Nickel Based Superalloy Gas Turbine Component, *Adv. Mater. Res.*, 2017, **17**(2), p 55–63
3. X. Ni, D. Kong, L. Zhang, C. Dong, J. Song, and W. Wu, Effect of Process Parameters on the Mechanical Properties of Hastelloy X Alloy Fabricated by Selective Laser Melting, *J. Mater. Eng. Perform.*, 2019, **28**(9), p 5533–5540. https://doi.org/10.1007/s11665-019-04275-w
4. N. Aminipour and R. Derakhshandeh-Haghighi, The Effect of Weld Metal Composition on Microstructural and Mechanical Properties of Dissimilar Welds Between Monel 400 and Inconel 600, *J. Mater. Eng. Perform.*, 2019, **28**(10), p 6111–6124. https://doi.org/10.1007/s11665-019-04328-0
5. R. Sihotang, P. Sung-Sang, and B. Eung-Ryul, Effects of Heat Input on Microstructure of Tungsten Inert Gas Welding Used Hastelloy X, *Mater. Res. Innov.*, 2014, **18**(sup2), p S2-1074–S2-1080. https://doi.org/10.1179/1432891714z.000000000559
6. R. Sihotang, S. Choi, S. Park, and E. Baek, Fatigue Life of the Repair TIG Welded Hastelloy X Superalloy, *J. Weld. Join.*, 2015, **33**(5), p 26–30. https://doi.org/10.5781/JWJ.2015.33.5.26
7. M. Pakniat, F.M. Ghaini, and M.J. Torkamany, Hot Cracking in Laser Welding of Hastelloy X with Pulsed Nd:YAG and Continuous Fiber Lasers, *Mater. Des.*, 2016, **106**, p 177–183. https://doi.org/10.1016/j.matdes.2016.05.124
8. J.C. Zhao, M. Larsen, and V. Ravikumar, Phase Precipitation and Time-Temperature-Transformation Diagram of Hastelloy X, *Mater. Sci. Eng. A*, 2000, **293**(1), p 112–119
9. M. Reza Abedi, H. Sabet, and H. Razavi, The Effect of Repair Welding Number on Microstructure of Hastelloy X Fabricated via TIG Process, *Int. J. Mater. Sci. Appl.*, 2016, **5**(2), p 43–48. https://doi.org/10.11648/j.ijmsa.20160502.12
10. S.G.K. Manikandan, D. Sivakumar, K. Prasad Rao, and M. Kamaraj, Effect of Weld Cooling Rate on Laves Phase Formation in Inconel 718 Fusion Zone, *J. Mater. Process. Technol.*, 2014, **214**(2), p 358–364. https://doi.org/10.1016/j.jmatprotec.2013.09.006
11. P. Subramani and M. Manikandan, Development of Welding Technique to Suppress the Microsegregation in the Aerospace Grade Alloy 80A by Conventional Current Pulsing Technique, *J. Manuf. Process.*, 2018, **34**(April), p 579–592
12. B. Arulmurugan and M. Manikandan, Development of Welding Technology for Improving the Metallurgical and Mechanical Properties of 21st Century Nickel Based Superalloy 686, *Mater. Sci. Eng. A*, 2017, **691**, p 126–140. https://doi.org/10.1016/j.msea.2017.03.042
13. S. Krishnan, D.V. Kulkarni, and A. De, Probing Pulsed Current Gas Metal Arc Welding for Modified 9Cr-1Mo Steel, *J. Mater. Eng. Perform.*, 2015, **24**(4), p 1462–1470
14. K. Pal and S.K. Pal, Effect of Pulse Parameters on Weld Quality in Pulsed Gas Metal Arc Welding: A Review, *J. Mater. Eng. Perform.*, 2011, **20**(6), p 918–931
15. D. Tomus, Y. Tian, P.A. Rometsch, M. Heilmaier, and X. Wu, Influence of Post Heat Treatments on Anisotropy of Mechanical Behaviour and Microstructure of Hastelloy-X Parts Produced by Selective Laser Melting, *Mater. Sci. Eng. A*, 2016, **667**(4), p 42–53. https://doi.org/10.1016/j.msea.2016.04.086
16. P. Subramani and M. Manikandan, Development of Gas Tungsten Arc Welding Using Current Pulsing Technique to Preclude Chromium Carbide Precipitation in Aerospace-Grade Alloy 80A, *Int. J. Miner. Metall. Mater.*, 2019, **26**(2), p 210–221
17. S. Sharma, R.V. Taiwade, and H. Vashishtha, Effect of Continuous and Pulsed Current Gas Tungsten Arc Welding on Dissimilar Weldments Between Hastelloy C-276/AISI, 321 Austenitic Stainless Steel, *J. Mater. Eng. Perform.*, 2017, **26**, p 1146–1157
18. K.S. Bal, J. Dutta Majumdar, and A. Roy Choudhury, Elemental Micro-segregation Characteristic of Fiber Laser Welded Hastelloy C-276 Sheet, *Trans. Nonferrous Met. Soc. China (English Ed)*, 2018, **28**(11), p 2236–2247. https://doi.org/10.1016/s1003-6326(18)64868-x
19. K. Wu, N. Ding, T. Yin, M. Zeng, and Z. Liang, Effects of Single and Double Pulses on Microstructure and Mechanical Properties of Weld Joints during High-Power Double-Wire GMAW, *J. Manuf. Process.*, 2018, **35**, p 728–734. https://doi.org/10.1016/j.jmapro.2018.08.025
20. F. George Vander Voort, *Metallography and Microstructures, ASM Handbook*, ASM International, Cleveland, 2004
21. E. Farahani, M. Shamanian, and F. Ashrafizadeh, A Comparative Study on Direct and Pulsed Current Gas Tungsten Arc Welding of Alloy 617, *AMAE Int. J. Manuf. Mater. Sci.*, 2012, **02**(01), p 1–6
22. A. Srikanth and M. Manikandan, Development of Welding Technique to Avoid the Sensitization in the Alloy 600 by Conventional Gas Tungsten Arc Welding Method, *J. Manuf. Process.*, 2017, **30**, p 452–466. https://doi.org/10.1016/j.jmapro.2017.10.014
23. K. Mageshkumar, P. Kuppan, and N. Arivazhagan, Characterization of Microstructure and Mechanical Properties of Nickel Based Superalloy 617 by Pulsed Current Gas Tungsten Arc Welding Technique, *Mater. Res. Exp.*, 2018, **5**(6), p 66541. https://doi.org/10.1088/2053-1591/aacb56
24. Y.T. Long, P.L. Nie, Z.G. Li, J. Huang, X. Li, and X.M. Xu, Segregation of Niobium in Laser Cladding Inconel 718 Superalloy, *Trans. Nonferrous Met. Soc. China (English Ed)*, 2016, **26**(2), p 431–436. https://doi.org/10.1016/s1003-6326(16)64131-6
25. Y.S. Sato, P. Arkom, H. Kokawa, T.W. Nelson, and R.J. Steel, Effect of Microstructure on Properties of Friction Stir Welded Inconel Alloy 600, *Mater. Sci. Eng. A*, 2008, **477**(1–2), p 250–258
26. M. Manikandan, N. Arivazhagan, M. Nageswara Rao, and G.M. Reddy, Microstructure and Mechanical Properties of Alloy C-276 Weldments Fabricated by Continuous and Pulsed Current Gas Tungsten Arc Welding Techniques, *J. Manuf. Process.*, 2014, **16**(4), p 563–572
27. K. Feng, P. Liu, H. Li, S. Sun, S. Xu, and J. Li, Microstructure and Phase Transformation on the Surface of Inconel 718 Alloys Fabricated by SLM under 1050 C Solid Solution + Double Ageing, *Vacuum*, 2017, **145**, p 112–115. https://doi.org/10.1016/j.vacuum.2017.08.044
28. M. Szkodo and G. Gajowiec, Studies of the Mechanism of Metal Dusting of 10CrMo9-10 Steel after 10 Years of Operation in the Semi-Regenerative Catalytic Reformer, *Corros. Sci.*, 2016, **102**, p 279–290. https://doi.org/10.1016/j.corsci.2015.10.016
29. D. William Callister, *Fundamentals of Materials Science and Engineering*, 5th ed., W. Anderson, Ed., Wiley, Ne York, 2001,
30. H. Wang, S. Wang, P. Gao, T. Jiang, X. Lu, and C. Li, Microstructure and Mechanical Properties of a Novel Near-α Titanium Alloy Ti6.0Al4.5Cr1.5Mn, *Mater. Sci. Eng., A*, 2016, **672**, p 170–174. https://doi.org/10.1016/j.msea.2016.06.083
31. Y. Guo, T. Jiang Li, C. Xia Wang, S. Fang Hou, and B. Han Wang, Microstructure and Phase Precipitate Behavior of Inconel 740H During Aging, *Trans. Nonferrous Met. Soc. China (English Ed.)*, 2016, **26**(6), p 1598–1606. https://doi.org/10.1016/s1003-6326(16)64266-8
32. M. Yousefieh, M. Shamanian, and A. Saatchi, Optimization of Experimental Conditions of the Pulsed Current GTAW Parameters for Mechanical Properties of SDSS UNS S32760 Welds Based on the Taguchi Design Method, *J. Mater. Eng. Perform.*, 2012, **21**(9), p 1978–1988
33. M. Balasubramanian, V. Jayabalan, and V. Balasubramanian, Effect of Microstructure on Impact Toughness of Pulsed Current GTA Welded α-β Titanium Alloy, *Mater. Lett.*, 2008, **62**(6–7), p 1102–1106

Publisher's Note Springer Nature remains neutral with regard to jurisdictional claims in published maps and institutional affiliations.